Full length article

Mechanical properties and deformation mechanisms of a Ni$_2$Co$_1$Fe$_1$V$_{0.5}$Mo$_{0.2}$ medium-entropy alloy at elevated temperatures

Wei Jiang[a], Shengyun Yuan[b], Yang Cao[a,*], Yong Zhang[b,*], Yonghao Zhao[a,*]

[a] Nano and Heterogeneous Materials Center, School of Materials Science and Engineering, Nanjing University of Science and Technology, Nanjing 210094, China
[b] Herbert Gleiter Institute of Nanoscience, Nanjing University of Science and Technology, Nanjing 210094, China

ABSTRACT

A Ni$_2$Co$_1$Fe$_1$V$_{0.5}$Mo$_{0.2}$ medium-entropy alloy (MEA) with a single-phase face-centered cubic (fcc) crystal structure are casted. The as-cast MEA possesses remarkable work hardening ability, yield strength (σ_y), ultimate tensile strength (σ_{UTS}) and uniform elongation (σ_u) at high temperatures up to 800 °C. Up-turn of strain hardening rate after elasto-plastic transition (secondary strain hardening) is observed for the MEA during tensile deformation in the temperature range of 25-800 °C. A high density of dislocation forests with solute atmospheres in concentrated solid solution is considered sufficient for back stress strengthening, thus causing the up-turn of strain hardening rate. Post-mortem microstructural analysis reveals that the temperature effects on mechanical properties of the MEA are closely related to dislocation structures, dislocation densities and dynamic-strain aging (DSA). With increasing deformation temperature from 25 °C to 800 °C, the dislocation density undulates and the fraction of screw dislocations increases. Strong solute pinning effect in conjunction with dominant forest strengthening mechanism (indicated by negative strain rate sensitivity and large activation volume) boost the strain hardening rate at the temperatures from 400 °C to 700 °C. At 800 °C, the dominant deformation mechanism changes from the forest dislocation cutting mechanism to dislocation cross-slip with increasing strain, resulting in the sharp up-turn of strain hardening rate. On the other hand, DSA poses plastic instability to deteriorate the strain hardening of the MEA. These phenomena are considered to have material impacts on mechanical properties and fracture mechanisms of MEAs and high-entropy alloys at high temperatures.

© 2021 Acta Materialia Inc. Published by Elsevier Ltd. All rights reserved.

1. Introduction

Seeking for materials with outstanding combinations of mechanical properties and a wide range of applications, has been a long-lasting endeavor for the materials community. While alloys of dilute solid solutions are still being researched and developed, there is an ongoing rush worldwide in researching alloys of concentrated solid solutions – medium-entropy alloys (MEAs) and high-entropy alloys (HEAs) [1-5]. MEAs contain three or more principal elements in near-equal atomic ratios [2], and their configurational entropies are in the range between 1R and 1.5R (R = 8.314 J · mol^{-1} · K^{-1}). HEAs usually contain five or more principal elements in near-equal atomic ratios [6-8], and their configurational entropies are larger than 1.5R [9]. Both MEAs and HEAs are concentrated crystalline solid solutions, in which atoms of various sizes are homogeneously distributed in the ideal situation. However, enthalpic interactions inevitably alter the local chemical order (LCO) in MEAs and HEAs, resulting in short range ordering (SRO) and/or incipient concentration waves [4,10,11]. In despite of the uncertainty of LCO, mixture of atoms of various sizes poses frequent short-range resistance to dislocation slip, thus to maximise the solid solution strengthening effect in MEAs and HEAs [3,12-16].

To date, it has been widely proven that both MEAs and HEAs possess outstanding low temperature mechcanical properties that are comparable to the very best cryogenic steels [5]. However, our understanding about the high temperature effect on the mechanical properties of MEAs and HEAs are still limited. According to literatures, almost all the MEAs and HEAs tend to loss both strength and ductility at elevated temperatures. In addtion, the majority of the MEAs and HEAs cannot sustain high strength and ductility at the temperature above 800 °C, including the prototypical CoCrFeNiMn HEA [17-20], the AlCuCrFeNiCo HEA with body centered-cubic (bcc) [21] and the Al$_{10}$Co$_{25}$Cr$_8$Fe$_{15}$Ni$_{36}$Ti$_6$ HEA [22]. In a general sense, the unsatisfactory mehcanical properties of MEAs and HEAs at elevated temperatures have so far been attributed to many factors including lowered lattice friction, lowered solute pinning

* Corresponding authors:
  E-mail addresses: y.cao@njust.edu.cn, cao_yang_leo@hotmail.com (Y. Cao), yong@njust.edu.cn (Y. Zhang), yhzhao@njust.edu.cn (Y. Zhao).

effect [23], lowered grain boundary (GB) strength, GB embrittlement, lowered strain hardening rate, dynamic-strain aging (DSA) induced stress instability and accelerated recovery/recrystallisation [24]. However, in order to quantify the effects of the abovementioned factors on mechanical properties, the governing deformation mechanisms have to be known [25,26]. Notwithstanding, the limited results are not yet enough to uncover the full protential of MEAs and HEAs, this is also the reason why increasing attentions are being paid to this research area.

In fact, all the factors affacting the high temperature mehcanical properties of MEAs and HEAs have long been considered in the developmemnt of conventional high-temperature alloys. Hence, examining the materials strengthening strategies used in conventional high-temperature materials can provide clue for strengthening MEAs and HEAs at high temperatures. Widely used conventional high-temperature materials are nickel-based superalloys [27-29], single- and poly-crystalline TiAl intermetallic compounds [30,31], heat-resistant steels [32,33] and oxide dispersion-strengthened (ODS) steels [34,35]. Nickel-based superalloys gain ultra-high strength from high densities nano-sized γ' precipitates and carbides [28], but meanwhile they need to face the challenge of limited ductility and embrittlement due to rapid coarsening of the γ' precipitates beyond 650 °C [27]. For the popular TiAl intermetallic compounds, their high strength is attributed to the fine dual-phase structure and the high content of β-stabilizing alloying elements, such as Nb and Mo [30,31,36,37]. Heat-resistant steels are the most widely used high-temperature materials for service temperatures of 550-600 °C. The high temperature mechanical properties of heat-resistant steels can be attributed to solid solutes W and Mo, and precipitations with V, Ti and Nb. However, the mechanical properties of heat-resistant steels deteriorate drastically with increasing temperature above 600 °C [32-35], due to precipiation of brittle carbides and/or phase transformation [38]. After examining these conventional high-temperature materials, it is realized that stable secondary phases, thermally stable precipitates and solutes of high melting points are key strategies for improving the strength of high-temperature materials. Since formation of secondary phases and precipitates decreases the configurational entropies, adding solutes of high melting points seems to be the primary option for improving the high temperature strength of MEAs and HEAs without lowering the entropies [39].

In this study, we prepared a non-equiatomic face-centered cubic (fcc) $Ni_2Co_1Fe_1V_{0.5}Mo_{0.2}$ MEA with severe lattice distortion by having Mo and V atoms. This MEA has been previously reported in only a few literatures [39,40]. As mentioned earlier, both Mo and V are common alloying elements for high-temperature materials, due to their high melting points, solid solution strengthening effect and phase stabilizing effect. The special multi-principal element design grants the MEA outstanding combination of strength and ductility at high temperatures up to 800 °C. Based on in-depth analysis of microstructures and mechanical behaviors, the mechanical properties and deformation mechanisms of the MEA at elevated temperatures are uncovered to exhaustive details. The evolution of dislocation density and variation of dislocation configuration with increasing temperature are deemed to have governing effect on the plastic flow of the $Ni_2Co_1Fe_1V_{0.5}Mo_{0.2}$ MEA.

2. Experimental

High purity (>99.5%) Ni, Co, Fe and V, Mo powders were melted in a boron nitride crucible by a medium frequency vacuum induction furnace, to make the $Ni_2Co_1Fe_1V_{0.5}Mo_{0.2}$ MEA ingot. The boron nitride crucible was heated at 600 °C for 1 hour to remove water vapor, before it was placed in the furnace. The furnace chamber was evacuated to 10^{-2} Pa and backfilled with argon to 0.06 MPa before the melting process. The liquid alloy was held at

1550 °C for 15 min, and poured into a ZrO_2-coated MgO crucible which was preheated at 600 °C. An IRTM-2CK infrared pyrometer was used to monitor the temperature with an absolute accuracy of 2 °C. The alloy was re-melted twice to ensure compositional homogeneity.

Dog-bone shaped tensile specimens with a gauge length of 16 mm and a diameter of 4 mm were cut from the ingot. The Instron 5982 tensile testing machine was used for tensile tests in the temperature range between 25 °C and 1000 °C. For tensile tests at elevated temperatures, the temperature was increased at a step size of ~30 °C /min until the desired temperature was reached. The samples were then held at the testing temperature for ~30 min before the start of the test. For quasi-static tensile tests, a constant strain rate of 1×10^{-3} s^{-1} was used. For strain rate jump tests, the strain rate was changed between 10^{-2} s^{-1} and 10^{-4} s^{-1} in a binary sense, during the continuously tensile loading.

Scanning electron microscopy (SEM), electron back-scattered diffraction (EBSD), energy dispersive spectroscopy (EDS), X-ray diffraction (XRD) and transmission electron microscopy (TEM) techniques were used to analyze the microstructure and composition of the material. A high-resolution field emission Carl Zeiss-Auriga-45 scanning electron microscope equipped with a fully automatic Oxford Instruments Aztec 2.0 EBSD system (Channel 5 software) was used for SEM and EBSD analysis. The EBSD specimens were mechanically polished and subsequently electropolished in an electrolyte containing 90 vol.% acetic acid and 10 vol.% perchloric acid with 35 V applied voltage and ~45 s polishing period in a Buehler ElectroMet-4 polisher. The same EBSD specimens were also used for EDS and XRD analysis. TEM observations were conducted in a FEI-Tecnai G^2 20 S-TWIN microscope operating at 200 kV. The TEM specimens were prepared by the standard procedure [41]. A bulk sample was machined and ground into a thin sheet of 50 μm thickness. Thin disks with a diameter of 3 mm were punched off the thin sheet. Each disk was electro-polished in a twin jet electro-polishing system containing an aqueous electrolyte of 10% perchloric acid, 20% glycerol and 70% methanol at -20°C, until a central perforation was observed.

3. Results

3.1. Initial Microstructures and Mechanical Properties

The as-cast $Ni_2Co_1Fe_1V_{0.5}Mo_{0.2}$ MEA has coarse grains of the sub-millimeter-scale, as shown in Fig. 1a. EDS maps (Fig. 1b) reveal that all the alloying elements (Ni, Co, Fe, V, Mo) are homogenously distributed in the area of study (300 × 400 μm^2), suggesting a single-phase solid solution without apparent elemental segregation or secondary phases. The XRD pattern (Fig. 1c) also reveals a single-phase fcc structure of the as-cast $Ni_2Co_1Fe_1V_{0.5}Mo_{0.2}$ MEA.

Mechanical behaviors for the as-cast $Ni_2Co_1Fe_1V_{0.5}Mo_{0.2}$ MEA within the wide temperature range of 25-1000 °C are illustrated in Fig. 2. As shown in Fig. 2a, the engineering stress-strain curves exhibit well-defined yield points at all testing temperatures. In the temperature range of 25-800°C, the MEA shows substantial strain hardening and excellent ductility. When the testing temperature is above 800°C, the MEA exhibits strain softening and significantly reduced ductility. It is worth noting that strong serrations present on the stress-strain curves in the temperature range of 400-800°C. The serration behavior will be addressed in detail in a later section.

Results of yield stress (σ_y), ultimate tensile strength (σ_{UTS}), uniform elongation (ε_u) and elongation to failure (ε_f) at different temperatures are summarized in Fig. 2b. Both strength and elongation of the MEA are strongly temperature-dependent. The yield strength decreases gradually from 310.7 MPa to 191.5 MPa as the temperature increases from 25°C to 900°C. When the temperature is in-
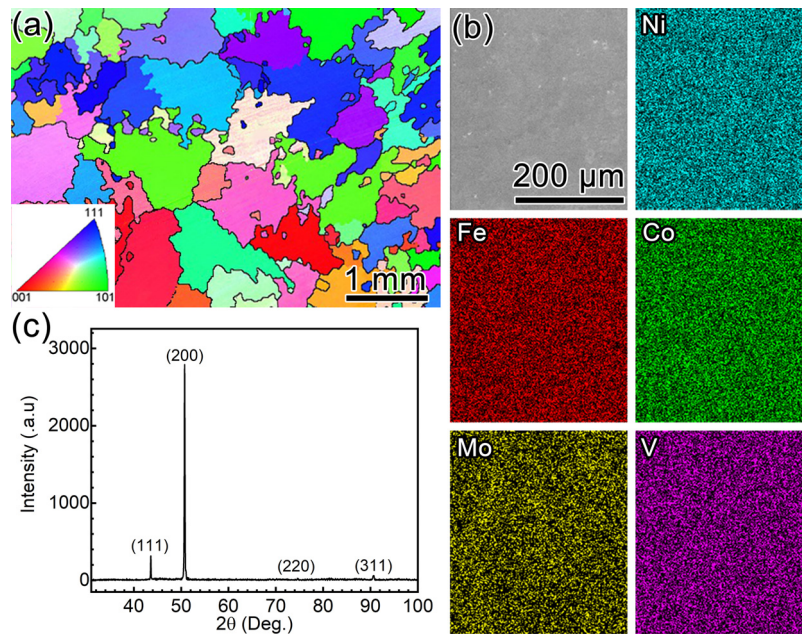
Fig. 1. Initial microstructures and compositional distributions of the as-cast $Ni_2Co_1Fe_1V_{0.5}Mo_{0.2}$ MEA. (a) An EBSD crystal orientation map showing near millimeter-size grains. (b) SEM-EDS maps showing homogeneous distributions of Ni, Co, Fe, V and Mo elements in the MEA. (c) The XRD pattern revealing the single-phase fcc structure of the as-cast MEA.
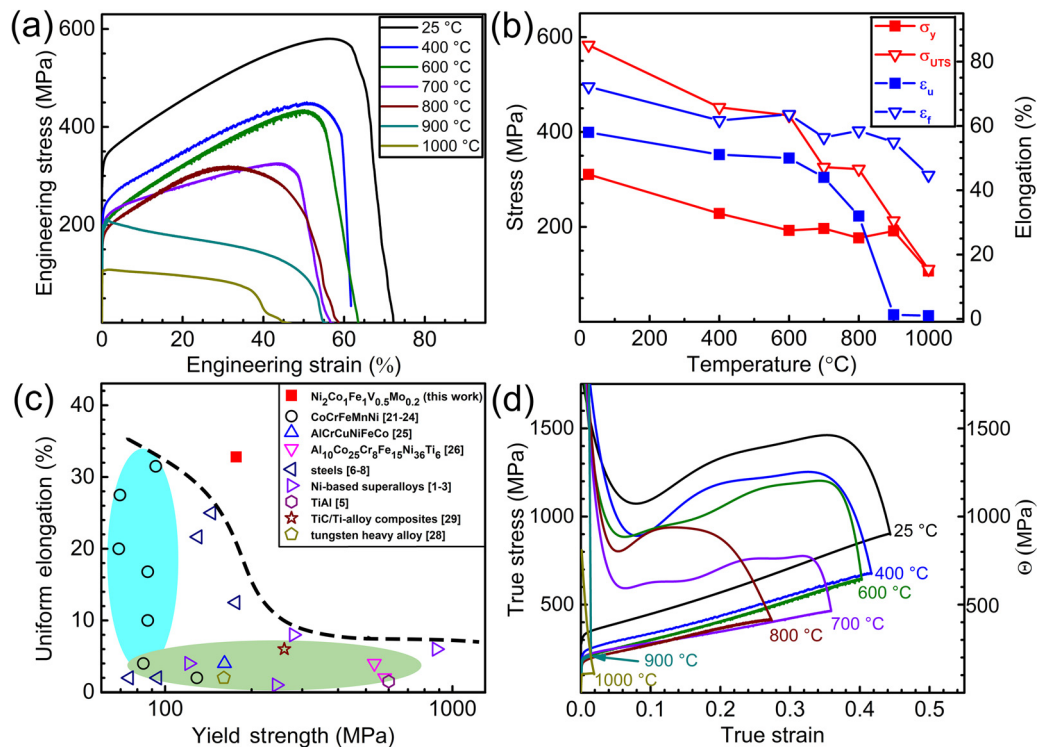

Fig. 2. Tensile properties of the $Ni_2Co_1Fe_1V_{0.5}Mo_{0.2}$ MEA: (a) Engineering stress-strain curves; (b) Yield stress, ultimate tensile strength, uniform elongation and elongation to failure versus temperature; (c) Comparison of this work and other high-temperature alloys for tensile properties at 800°C; (d) True stress and strain hardening rate versus true strain.

creased to 1000°C, the yield stress of the MEA drops dramatically to 107 MPa, indicating a thermal softening effect. Similarly, the ultimate tensile strength also decreases with increasing temperature. Eventually, the yield strength (red square) and the ultimate tensile strength (red triangle) overlapped at 900°C and 1000°C, indicating the lack of strain hardening capability at such high temperatures. On the other hand, the uniform elongation shows a gentle decline from 62% to 32% as the temperature increases from 25°C to 800°C.

At 900°C and 1000°C, the MEA samples show necking immediately after yielding, leading to negligible uniform elongations. The elongation to failure shows a gradual drop from 73% to 47% as the temperature increases from 25°C to 1000°C.

Fig. 2c summarizes uniform elongation vs. yield strength of the $Ni_2Co_1Fe_1V_{0.5}Mo_{0.2}$ MEA and typical high-temperature alloys tested at 800°C. As shown in Fig. 2c, many of the data points are located at the bottom left corner of the chart, this is be-
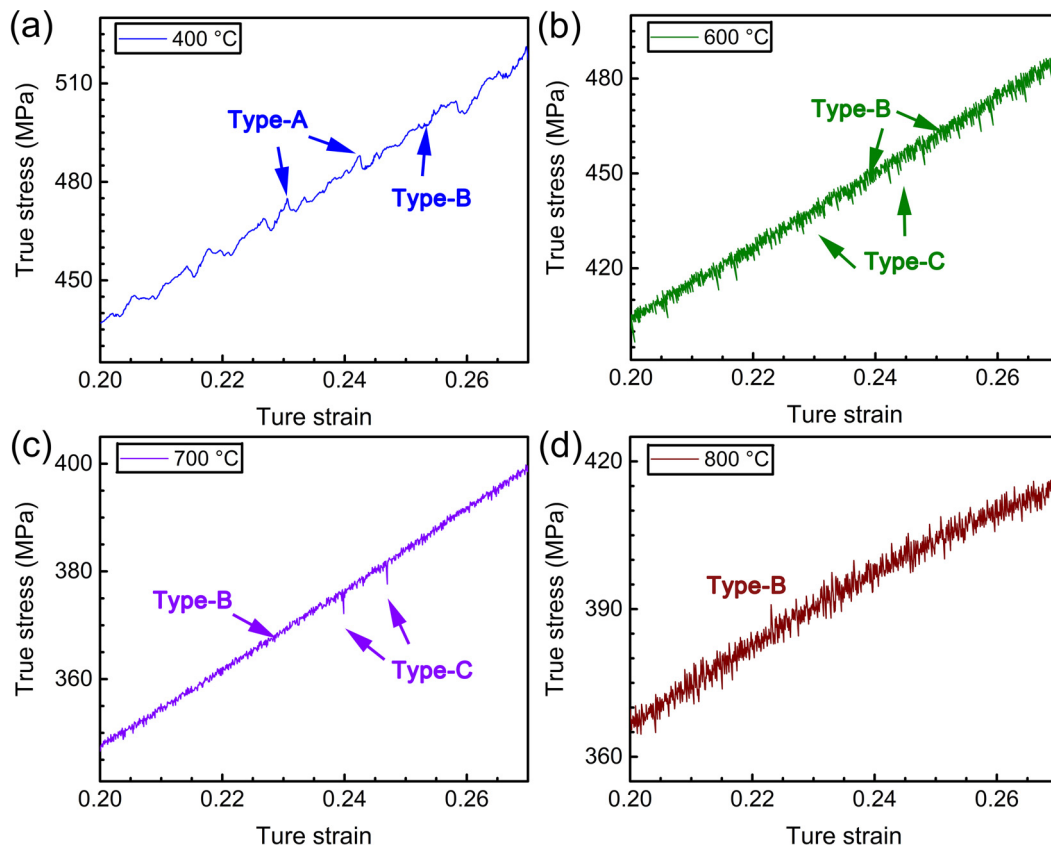
Fig. 3. Enlarged segments of true stress-strain curves in Fig. 2d. (a) The flow behavior at 400 °C features both type-A and type-B serrations. (b) The flow behavior at 600 °C features both type-B and type-C serrations. (c) The flow behavior at 700 °C features mainly type-B serrations and occasionally some type-C serrations. (d) The flow behavior at 800 °C features type-B serrations only.

cause the majority of these high-temperature alloys experience severe thermal softening and thus have low or even negligible strain hardening capabilities at 800°C. These high-entropy alloys and conventional high-temperature alloys (steels, Ni-based superalloy, TiAl etc.) display a strength-ductility trade-off trend below the dash line in Fig. 2c [17-22,27-29,31-34,42-44]. The presently studied MEA encouragingly breaks the usual strength-ductility paradox and show outstanding combination of uniform elongation and yield strength at 800°C. Fig. 2d is the true stress-strain curves and the corresponding strain hardening rate (Θ) curves for the $Ni_2Co_1Fe_1V_{0.5}Mo_{0.2}$ MEA at various temperatures. The strain hardening rate curve of the $Ni_2Co_1Fe_1V_{0.5}Mo_{0.2}$ MEA displays a large profile of up-turn in the strain range of ~0.1 to ~0.4, at the test temperature of 25°C. The size of the up-turn profile decreases with increasing temperature from 25°C to 700°C. Interestingly, the up-turn profile shows much higher strain hardening rates at 800°C than at 700°C. At 900°C and 1000°C, the material has lost strain hardening capability. Thus, the true stress-strain curve intercept with the strain hardening rate-true strain curve at low strain, when the test temperature is at 900°C and higher, suggesting the early onset of necking.

Fig. 3 shows enlarged segments of true stress-strain curves in Fig. 2d to demonstrate the evolution of serrations with increasing temperature. It is evident from Fig. 2a and Fig. 3 that serrated flow is apparent in the temperature range of 400-800°C. The serrated flow behaviors found by the high temperature tensile tests can be categorized into three types. The type-A serrations show upward spikes above the average serration amplitude, as shown in Fig. 3a. The type-B serrations have uniform frequency and amplitude, as shown in all four charts in Fig. 3. The type-C serrations feature downward spikes (stress drops) as shown in both Fig. 3b and c.

The types of serrations are associated with deformation mechanisms and solute drag effects. Thus, changing of serration types with increasing temperature indicates the changes of deformation mechanism and diffusion.

An important parameter used for evaluating the extent of strain hardening is the strain hardening exponent *n*, which can be deduced by the Ludwick ($\sigma_t = \sigma_y + K\varepsilon_p^n$) equation. The symbols σ_t, σ_y, K and ε_p denote true stress, yield strength, strengthening coefficient and true strain, respectively. Fig. 4a-e display the experimental results and the true plastic strain curves simulated by the Ludwick equation at different temperatures. Close examination of the experimental stress-strain curves reveals that the curves obtained at 25°C, 400°C, 600°C, 700°C and 800°C concave down slightly within the strain range between 0.05 and 0.4. The concaved stress-strain curves are attributed to the up-turn of strain hardening rate. Fig. 4f shows the variation of *n* with respect to temperature. The strain hardening exponent is an indicator for the strain hardening capability or formability of the material. Thus, Fig. 4f shows that the strain hardening capability (strain hardening exponent) of $Ni_2Co_1Fe_1V_{0.5}Mo_{0.2}$ MEA decreases slightly with increasing temperature from 25°C to 600°C, and then drops sharply with increasing temperature from 600°C to 700°C. It is worth to note that the strain hardening exponent of the MEA decreased very slightly from 0.92 to 0.90, when the temperature increased from 700°C to 800°C. There is no data point for 900°C and 1000°C tests, because the sample materials have lost strain hardening capability at such high temperatures. The variation of the strain hardening exponent against temperature (Fig. 4f) is consistent with that of the strain hardening rate (Fig. 2d).

As shown in Fig. 2a and d, the samples tested at 800 °C exhibit higher strain hardening rates than those tested at 700 °C at
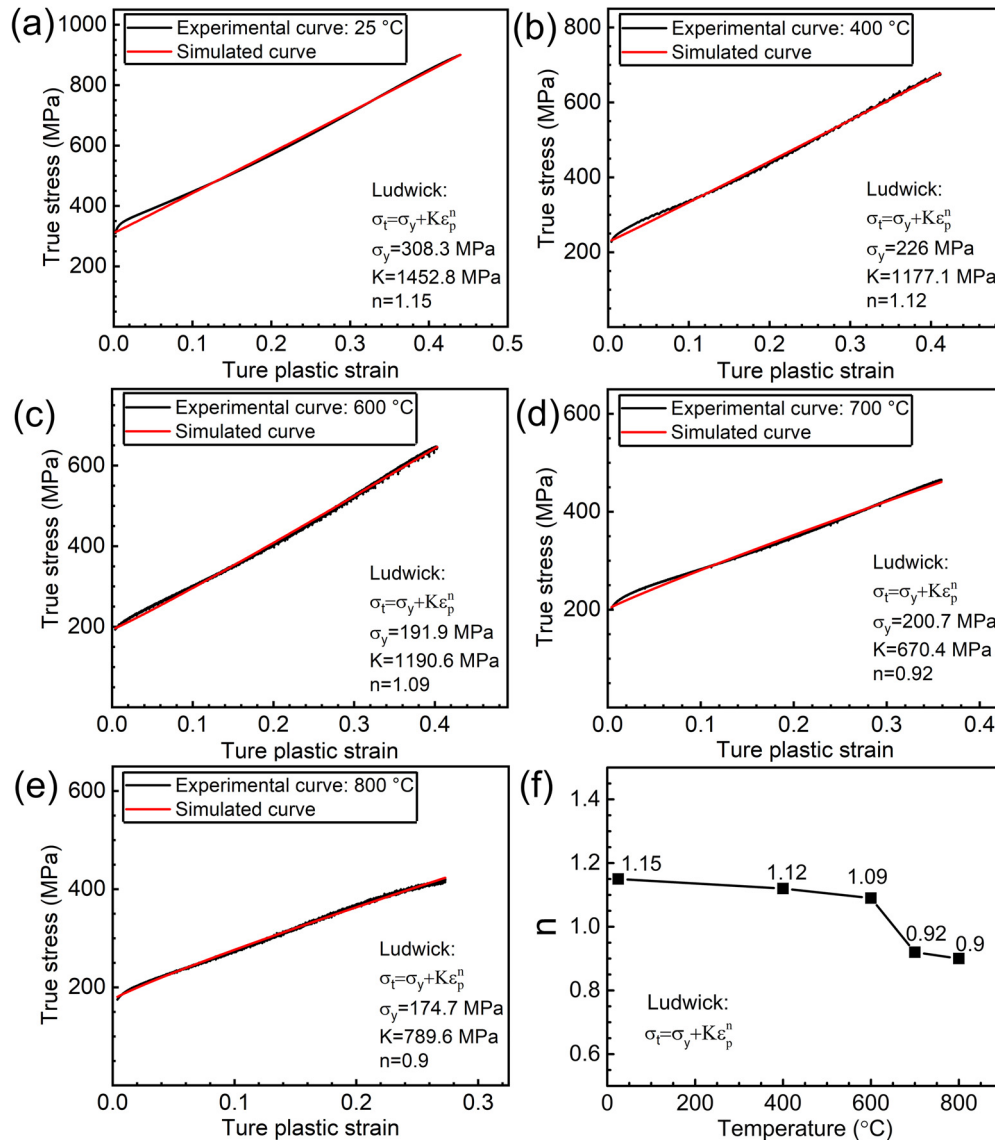
Fig. 4. Experimental true stress versus true plastic strain curves of the $Ni_2Co_1Fe_1V_{0.5}Mo_{0.2}$ MEA and simulated curves (by Ludwick equation) at different temperatures: the test temperatures are at (a) 25°C, (b) 400°C, (c) 600°C, (d) 700°C and (e) 800°C. (f) Strain hardening exponent n versus temperature.

the low strain level. In order to understand this unexpected phenomenon and the related strain hardening mechanisms, thermal activation processes and strain rate sensitivities (SRSs) of the MEA are investigated in detail by strain rate jump tests at the temperature range between 25 °C and 800 °C. As shown in Fig. 5a, at the strain range of 5-25%, jump strain rates between 10^{-2} s^{-1} and 10^{-4} s^{-1} are used during tensile tests. The initial loading strain rate was 10^{-3} s^{-1}. At ~5% elongation the strain rate was increased to 10^{-2} s^{-1} and sustained for further ~2% elongation. Then the strain rate was decreased to 10^{-4} s^{-1} and sustained for further ~2% elongation. The strain rate is exchanged onward between 10^{-2} s^{-1} and 10^{-4} s^{-1} until the total tensile elongation of 25%. At 25 °C, the plastic flow is sensitive to strain rate in a way that increased strain rate leads to increased stress (positive SRS), and stress serrations are negligible. At the temperatures of 400°C, 600°C and 700°C, negative SRS can be noticed, that the stress decreased moderately upon the strain rate jump from 10^{-4} s^{-1} to 10^{-2} s^{-1}. Meanwhile, the amplitude of serrations decreased with increasing strain rate. Another distinct plastic flow behavior occurred at 800°C under the strain rate jump test. When the strain rate was increased to 10^{-2}

s^{-1}, the stress increased (positive SRS) and the amplitude of serrations reduced to a negligible level. When the strain rate was decreased to 10^{-4} s^{-1}, a sudden drop of stress occurred and then the stress fetched up moderately while the strain rate was held at 10^{-4} s^{-1}. As a result, strong fluctuations in stress were realized during the strain rate jump test at 800°C.

Plastic flow of metallic materials is fundamentally affected by thermally activated processes such as dislocation slip, deformation twinning, stacking faults (SFs), solute drag and diffusion [45]. In concentrated solid solutions such as HEAs and MEAs, discrete but not far-spaced solute atoms pose strong lattice frictions to dislocations and SFs, resulting in complicated plastic deformation processes at atomic scale. Hence, it is a common practice to use the generalized physical parameters, activation volume (ΔV^*) and SRS (m), to help exploring the underlying physics of the temperature dependent mechanical behaviors of HEAs and MEAs. Note that the activation volume is not a physical volume, it is better described as the coefficient of isostatic stress in affecting the activated event [46]. Based on the data collected from strain rate jump tests, an activation volume ΔV^* can be estimated by the equation [47,48]:
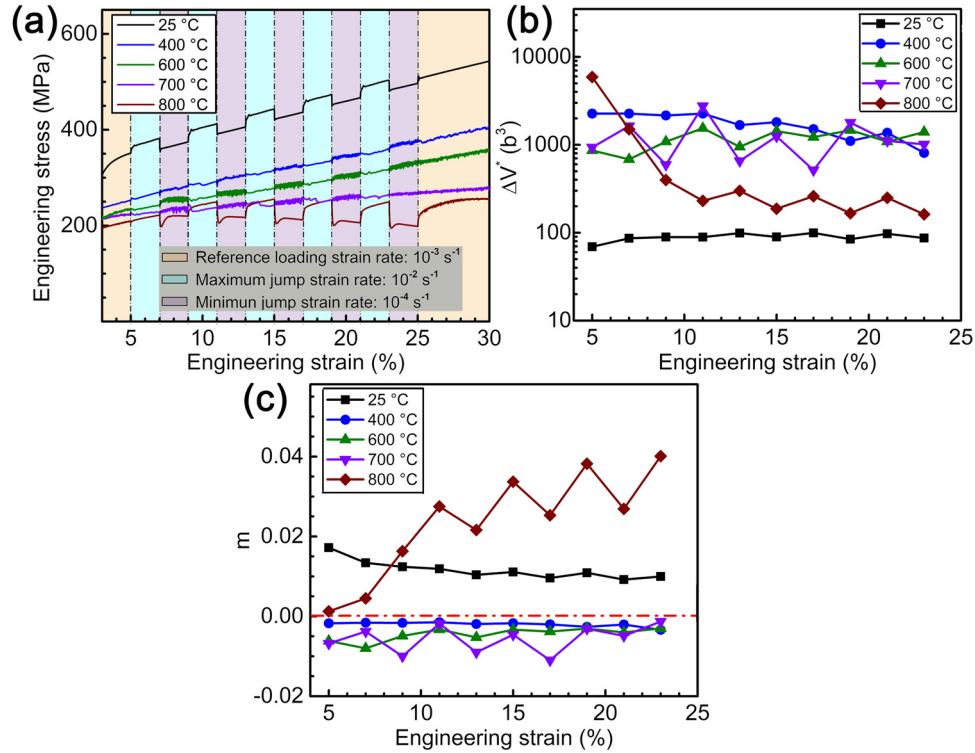
Fig. 5. (a) Engineering stress-strain curves obtained by strain rate jump tests at 10^{-2} s^{-1} and 10^{-4} s^{-1}. (b) Activation volume versus engineering strain. (c) SRS versus engineering strain.

$$\Delta V^* = \sqrt{3} k_B T \frac{\partial ln\dot{\varepsilon}}{\partial \sigma} \qquad (1)$$

Where k_B is the Boltzmann constant, T is the absolute temperature, σ is the normal flow stress and $\dot{\varepsilon}$ is normal strain rates. An activation volume is usually given in a normalized form $\Delta V^*/b^3$, in units of b^3 (in the current case b=0.254 nm is the magnitude of the Burgers vector for the Ni$_2$Co$_1$Fe$_1$V$_{0.5}$Mo$_{0.2}$ MEA).

The SRS can be estimated by the equation [48]:

$$m = \left(\frac{\partial ln\sigma}{\partial ln\dot{\varepsilon}} \right) \qquad (2)$$

Fig. 5b displays the activation volume versus engineering strain. At 25 °C, ΔV^* is comparatively low and steady within the range of 69 b^3 to 105 b^3. At elevated temperatures of 400°C, 600°C and 700°C, ΔV^* stays high within the range of 390 b^3 to 2760 b^3; As the temperature increases, the fluctuation of ΔV^* with increasing strain amplifies. Increasingly, at 800°C the ΔV^* is no longer steady, but decreases from 5910 b^3 to 162 b^3 with increasing strain.

The trend of SRS versus engineering strain is opposite to that of the activation volume versus engineering strain. As shown in Fig. 5c, at 25 °C, m is comparatively high and shows a moderate decreasing trend with increasing strain. At elevated temperatures of 400°C, 600°C and 700°C, m values are steady at the negative regime, but the fluctuation of m values amplifies as the temperature increases. At 800°C, m increases and fluctuates with increasing strain. At tensile strain larger than ~10, the SRS of the MEA is found higher at 800 °C than at 25 °C.

3.2. Deformation and fracture mechanisms

Post-mortem TEM analysis was carried out to reveal the deformation mechanisms of the Ni$_2$Co$_1$Fe$_1$V$_{0.5}$Mo$_{0.2}$ MEA at different temperatures. Fig. 6a shows a typical bright-field (BF) TEM micrograph and the corresponding selected area electron diffraction

(SAED) pattern of the sample tensile deformed at 25°C. The inserted SAED pattern was recorded at the [110] zone axis, but the BF TEM image was taken slightly off the zone axis in a two-beam condition to enhance the contrast of dislocations. Apparently, dislocation slip on {111} planes dominates the plastic deformation at 25°C. The majority of the dislocations appeared as long and straight lines parallel to (-111) and (1-11) slip planes, suggesting that planar slip is mostly confined on close-packed planes. The density of dislocations is as high as 22×10^{13} m^{-2} in the tensile deformed MEA at 25°C. As the temperature increases to 400°C and 600°C, dislocation interactions associated with cross-slip and climb become pronounced, evidenced by a large amount of curved dislocation lines that are unparallel to {111} planes (Fig. 6b). Interestingly, planar dislocation arrays and SFs are also found frequently in samples deformed at 400°C and 600°C, as illustrated in Fig. 6c. The coexistence of confined dislocation slip and cross-slip are attributed to interactions of high densities of dislocations [1] and Suzuki segregation [45]. The dislocation densities of the samples deformed at 400°C and 600°C are 15.7×10^{13} m^{-2} and 18.6×10^{13} m^{-2}, respectively. As the temperature increases to 700°C, long and straight dislocations, short and wavy dislocations (Fig. 6d), SFs (Fig. 6e) and dipole loops (Fig. 6f) become the dominant deformation structures. (The dipole character of the dislocation arrangement is revealed by the operating diffraction vector g = (002), as shown in Fig. 6f.) The dislocation density of the sample deformed at 700°C is approximately 20.1×10^{13} m^{-2}.

When the temperature is increased to 800 °C which is above $0.6T_m$, the shear modulus is lowered and the enthalpy is significantly increased [49]. As a result, the line tension of dislocations [50] and the activation energy for cross-slip are significantly reduced [51], leading to long and curved dislocations as shown in Fig. 7a and b. At such a high temperature, the free energy of mixing, the diffusivity of solute atoms and the number of vacancies is sufficiently high, resulting in homogenous distribution of solute atoms, and reduced tendency for Suzuki segregation and SRO.
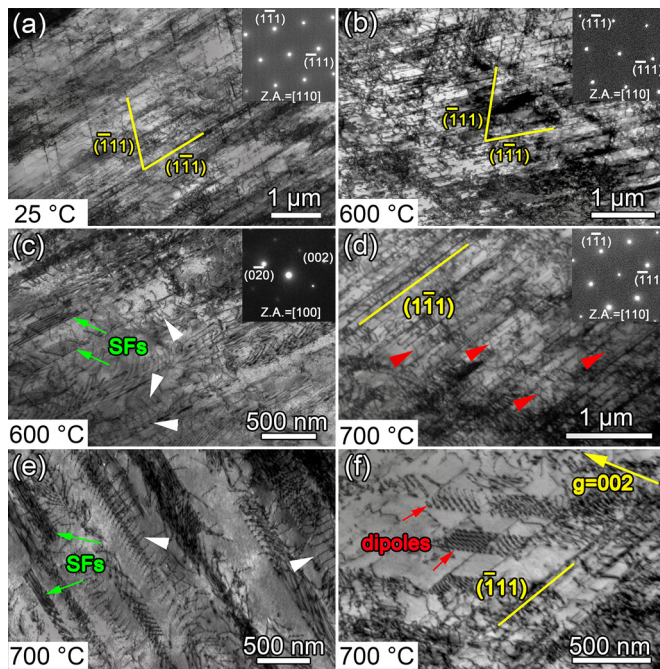
Fig. 6. BF-TEM images showing dislocation structures at the gauge sections of post-tensile test specimens. (a) Planar slip character verified by the intersecting trace of edge-on (-111) and (1-11) slip planes, in the sample deformed at 25 °C; (b)-(c) Typical dislocation structures and SFs (indicated by green arrows) in samples deformed at 600 °C; (d)-(f) Typical microstructures in samples deformed at 700 °C; Wavy dislocations are indicated by red triangles; Planar arrays of dislocations are indicated by white triangles; Dislocation dipoles are indicated by red arrows.

Fig. 8. A chart showing the change in dislocation density with respect to deformation temperature for the tensile deformed $Ni_2Co_1Fe_1V_{0.5}Mo_{0.2}$ MEA.

Hence, SFs and planar arrays are no longer found in the deformed sample. After tensile deformation, the density of dislocations is approximately $13.8 \times 10^{13}\ m^{-2}$.

At 900 °C which is about $0.7T_m$, both dislocation cross-slip mechanisms and diffusion-controlled recovery mechanisms dominate the plastic deformation process under the effect of shear stress and high temperature [51]. As a result, strong dynamic recovery occurred. Dislocations tangled and organized into low energy dislocation structures such as cell walls and sub-grain boundaries, as shown in Fig. 7c. Recrystallized grains with equiaxed
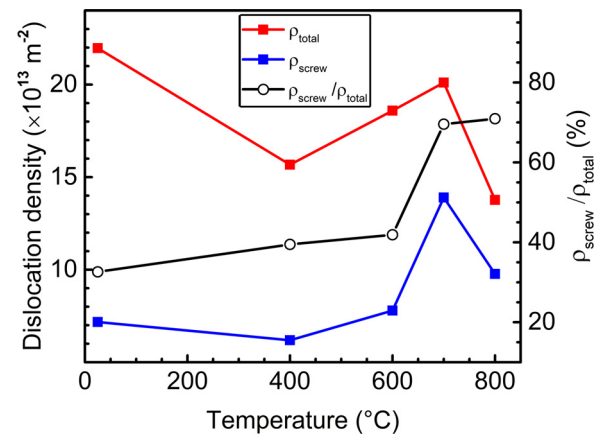
shape and sharp GBs are observed randomly, as shown in Fig. 7d, suggesting the deformation temperature is high enough to cause dynamic recrystallization. Thus, reasonably the flow stress is significantly lowered and strain hardening effect is diminished, as shown in Fig. 2a.

The dislocation densities were measured by a TEM method [52] at the necking regions of the MEA samples deformed at different temperatures. Detailed description and justification of the dislocation density measurement is provided in the supplementary material. As shown in Fig. 8, the total dislocation density is the highest when the sample was deformed at 25 °C. When the deformation temperature was increased to 400 °C, the dislocation density was lowered compared to that at 25 C. Interestingly, as the deformation temperature was increased further from 400 °C to 700 °C, the dislocation density also increased linearly. As the deformation temperature was increased to 800 °C which is above $0.6T_m$, the dislocation density inevitably decreased again due to strong recovery effect [51].

Edge and screw dislocations have different configurations [46], slip mechanisms and recovery mechanisms [53], thus their contributions to the flow stress and strain hardening are different especially for concentrated solid solutions. In order to explore the

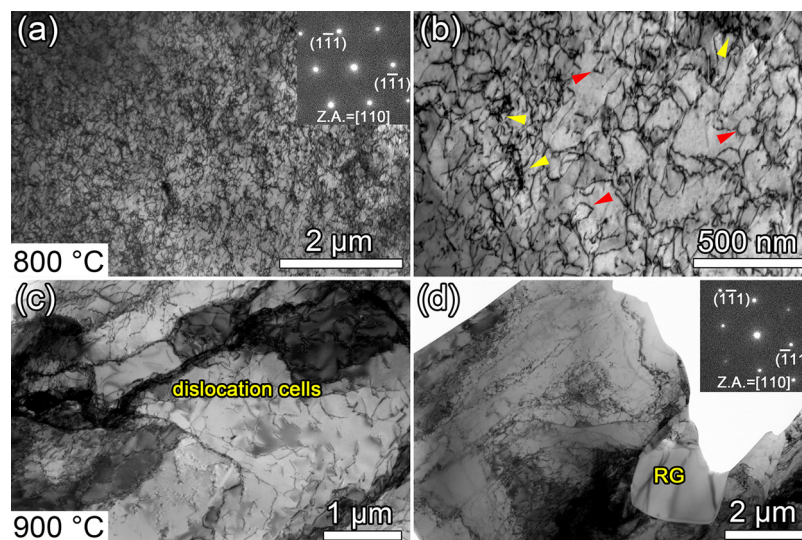**Fig. 7.** BF-TEM images showing dislocation structures at the gauge sections of post-tensile test specimens. (a)-(b) A high density of dislocations observed in the sample deformed at 800 °C; Wavy and curved dislocations are indicated by red triangles; Entangled dislocations are indicated by yellow triangles. (c) Dislocation cell structures and (d) a recrystallized grain (RG) found in the sample deformed at 900 °C.

flow behaviors of the MEA in-depth, the densities of screw dislocations are measured and plotted separately on Fig. 8. Unfortunately, it is difficult to distinguish between edge dislocations and mixed dislocations by TEM. Nevertheless, distinguishing the density of screw dislocations from total dislocation density can still provide important information about the temperature effect on flow behaviors. The density of screw dislocations is ~7.17×10^{13} m^{-2} at 25°C, and fluctuates moderately in the temperature range between 25 °C and 600 °C. When the test temperature is increased to 700 °C, the density of screw dislocations surprisingly increases to ~13.9×10^{13} m^{-2}. As the temperature is increased further from 700 °C to 800 °C, the density of screw dislocations decreases to ~9.8×10^{13} m^{-2}. It can be noticed that at the temperature below 600 °C, the screw dislocations account for less than 42% of the total number of dislocations, but when the temperature is above 700 °C, the fraction of screw dislocations increases to ~70%. Apparently, screw dislocations are strongly promoted over edge dislocations and mixed dislocations at high temperatures.

SRO is an important configurational feature that affects the deformation mechanisms of HEAs and MEAs. According to density functional theory based numerical results, SRO atomic configuration poses high energy barrier for dislocation slip. Thus, high shear stress is required to drive the leading dislocation to overcome the slip resistance. The leading dislocation can interrupt the SRO atomic configuration on its slip path, thus reduce the energy barrier for the dislocations gliding on the same path. Therefore, in the materials with SRO, dislocations tend to arrange in planar arrays that have often been found in HEAs and MEAs [11,20]. However, it is still a world class conundrum to directly visualize SRO [4,10,11]. Therefore, an indirect approach is made to assess the SRO in the samples deformed at different temperatures. Planar arrays (marked by white triangles in Fig. 6) are recognized as the sign of SRO [11,54]. After detailed TEM analysis on the samples deformed in the temperature range between 25 °C and 1000 °C. It is concluded that planar arrays are detectable in the samples deformed below 800 °C, as shown in Fig. 6 and Fig. S1a in the supplementary material. In contrast, as shown in Fig. 7a-b and Fig. S1b, the line-shapes and arrangement of dislocations in the $Ni_2Co_1Fe_1V_{0.5}Mo_{0.2}$ MEA deformed at 800 °C resembles dislocations in the plastically deformed pure Nickel (Fig. S1c). The major configurational difference between the $Ni_2Co_1Fe_1V_{0.5}Mo_{0.2}$ MEA and pure Nickel is the possible presence of SRO. At low temperatures, enthalpic interactions lead to SRO in concentrated solid solutions. When the temperature is sufficiently high, the entropy predominates the free energy reduction in concentrated solid solutions, thus random solid solution is preferred over SRO. Therefore, comparison of the dislocation arrangements in the $Ni_2Co_1Fe_1V_{0.5}Mo_{0.2}$ MEA and pure Nickel provides indirect evidence of SRO in $Ni_2Co_1Fe_1V_{0.5}Mo_{0.2}$ MEA at low to medium temperatures.

3.3. Fracture Morphologies

Fracture tip morphology was examined carefully by using SEM, to reveal the fracture modes. As shown in Fig. 9, all four samples failed under the ductile fracture modes within the temperature range between 25 °C and 700 °C. Side views of the fracture tips are shown in Fig. 9 a-1, b-1, c-1 and d-1. All four samples have blade-like fracture tips. The shear fracture angle θ (the angle between the fracture surface and tension axis) measured at the fracture tips are between 46° and 57°. Many wavy cracks are seen on the lateral surfaces of the tips. The cracks are thick on the samples fractured at 25 °C (Fig. 9 a-1) and 600 °C (Fig. 9 c-1), and are very fine on the samples fractured at 400 °C (Fig. 9 b-1) and 700 °C (Fig. 9 d-1). Fig. 9 a-2, b-2, c-2 and d-2 show top views of the fracture tips. Area reduction due to necking is clearly observable from all four samples. Fig. 9 a-3, b-3, c-3 and d-3 show

detailed surface morphology of the fracture tips in top views. Plastically formed dimples of various sizes are the major features on the fracture tips. Sizes and distributions of the dimples for samples tested at 25-600°C are very similar as shown in Fig. 9 a-3, b-3 and c-3. In contrast, the dimple sizes are larger in the sample tested at 700°C, as shown in Fig. 9 d-3. In addition, cleavage planes of various orientations are observed in Fig. 9 d-3, suggesting planar cleavage occurred during fracture.

At 800 °C, the shear fracture angle is $\theta = $ ~50°, and wavy cracks are very fine on the lateral surface, as shown in Fig. 10 a-1. This is similar to the fracture tips at lower temperature shown in Fig. 9. However, Fig. 10 a-2 and a-3 show that there are numerous fine spheres on the inner walls of the dimples. These fine spheres formed during fracture, due to dynamic recrystallization and partial melting of debris at the exposure of the fracture tip [21]. The local strain at the fracture surface can reach several times the global strain, meanwhile the Gibbs free energy at the fracture surface is significantly higher than that inside the bulk sample. TEM observations (Fig. 7a and b) did not detect recrystallization in the post tensile samples, but fine spheres due to recrystallisation and partial melting of the dimples are apparent on the fracture tip. This result suggests that 800 °C is very close to the threshold temperature for recrystallisation of the bulk $Ni_2Co_1Fe_1V_{0.5}Mo_{0.2}$ MEA under the quasi-static tensile deformation condition [21].

As shown in Fig. 10 b-1, the sample tested at 900 °C exhibits cup-cone shape fracture tip with a shear fracture angle of $\theta = $ ~90°. Wavy cracks on the lateral surface become very thick. As shown in Fig. 10 b-2 and b-3, numerous globules are observed on the fractured surface, indicating the occurrence of ductile fracture. The sizes of the globules are in the range of 10 – 20 μm at 900 °C. As shown in Fig. 10 c-1, the shear fracture angle of $\theta = $ ~90° obtained at 1000 °C is similar to that at 900 °C. However, wavy cracks are hardly seen on the lateral surface of the tip. The transverse area reduction is less discernible at 1000 °C than these at lower temperatures, as shown in Fig. 10 c-2. The sizes of the globules are as large as 60 μm, as shown in Fig. 10 c-3. Cracks on globules were formed when the tip was cooled from a high temperature, due to local strain incompatibility induced by thermal contraction.

4. Discussion

4.1. Temperature dependence of mechanical properties

Overall, the as-cast $Ni_2Co_1Fe_1V_{0.5}Mo_{0.2}$ MEA possesses an outstanding combination of strength and ductility at the test temperatures up to 800 °C, as shown in Fig. 2. As the deformation temperature increases from 25 °C to 1000 °C, both strength and ductility of the MEA decrease as a general trend. This is consistent with previously studied HEAs [55] and MEAs [25]. Loss of strength at elevated temperatures for both HEAs and MEAs are attributed to the combined effect of lowered lattice friction, lowered GB strength, lowered solute pinning effect [23] and accelerated recovery/recrystallisation [25]; Loss of ductility are attributed to lowered strain hardening rate, GB embrittlement and DSA induced stress instability [23,55]. While the temperature effect on mechanical properties of concentrated solid solution is determined by the many factors mentioned above, generalized parameters are helpful for discriminating the factors and finding the key issues that require attention.

Firstly, the variation of SRS with increasing temperature grabbed our attention. According to Hart's plastic instability criterion [56], enhanced SRS under a given flow stress will restrain strain localization, maintain uniform plastic deformation before necking and prevent abrupt fracture after necking, resulting in improved ductility. The SRS of pure fcc metals are insensitive to
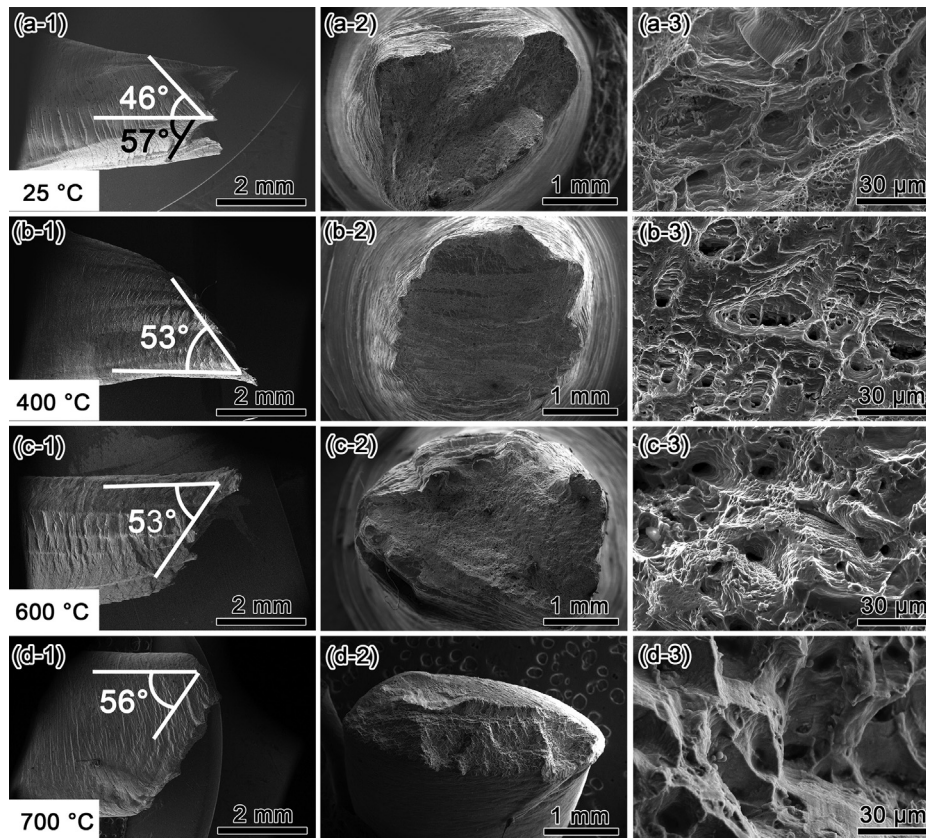
Fig. 9. SEM images showing the fracture tips of the post-tensile samples tested at (a) 25°C, (b) 400°C, (c) 600°C and (d) 700°C. Images in the first column are side views. Images in the second column are top views. Images in the third column are top views at a high magnification.

Fig. 10. SEM images showing fracture tips of the post-tensile samples tested at (a) 800°C, (b) 900°C and (c) 1000°C. Images in the first column are side views. Images in the second column are top views. Images in the third column are top views at a high magnification.
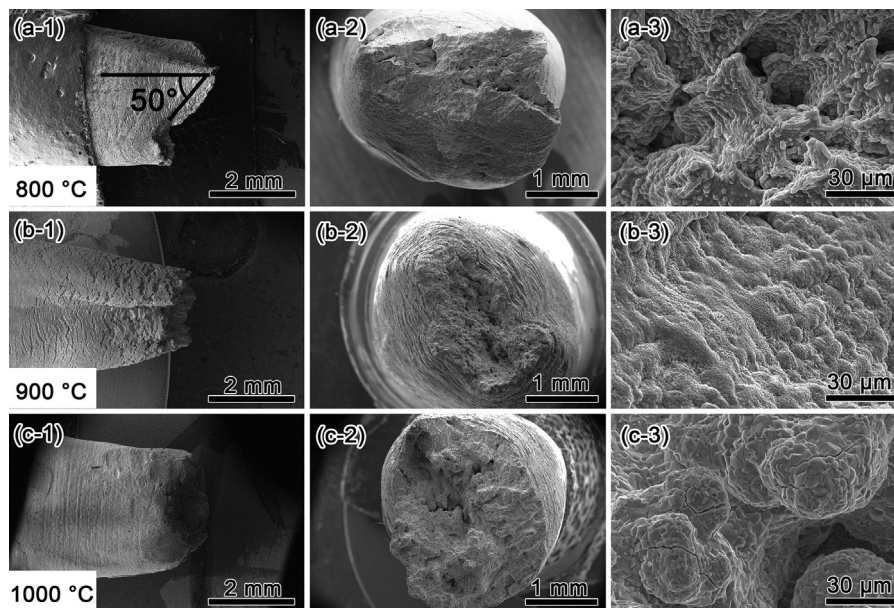
temperature within the low to medium homologous temperature range, due to negligible Peierls–Nabarro barriers; In contrast, for concentrated solid solutions, the Peierls barrier height decreases with increasing temperature due to LCO [4] and thermally induced increase of dislocation width, leading to reduced SRS [24]. In accordance, the inverse proportion between SRS and temperature is also observed for the $Ni_2Co_1Fe_1V_{0.5}Mo_{0.2}$ MEA deformed in the temperature range between 25 °C and 700 °C, as revealed in Fig. 5c. However, the SRS not only decreased with increasing temperature, but decreased into negative values in the temperature range between 400 °C and 700 °C. Moreover, at 800 °C, the SRS increased to the positive regime and increases with increasing strain, as revealed in

Fig. 5c. These two observations are attributed to DSA effects. DSA of forest dislocations can decrease the SRS to the negative region. In contrast, the solute drag effect acting on the unpinned mobile dislocations adds a positive SRS [25,57,58].

DSA is usually revealed by serrations of plastic flow which have been shown in Fig. 2a and Fig. 3. Three types of serrations exchanged dominance with the increasing temperature from 400 °C to 800 °C. Type-A serrations are associated with the repeated initiation and continuous propagation of macroscopic Portevin–Le Chatelier (PLC) deformation bands along the specimen gauge length [59]. Type-A serration occurs at comparatively low temperature at which dislocations are initially in the unlocked state within the PLC band. During plastic deformation, solute atoms diffuse to mobile dislocations arrested temporarily at obstacles such as forest dislocations to sharply increase the load. The solute locking is temporary, the sharp increase in local stress soon unlocks the mobile dislocations from solute atmospheres, resulting in a subsequent load drop. Hence the Type-A serrations feature upward spikes in the stress-strain plot [60], as shown in Fig. 3a. Type-B serrations are attributed to locking and unlocking of mobile dislocations in the discontinuously propagating PLC bands. Therefore, type-B serrations feature fine scale oscillations about the mean level of flow stress and usually occur at intermediate temperature. Type-B serrations are promoted by increased temperature or decreased strain rate, and the serrations have a high frequency and low magnitude, suggesting high diffusivity and fast diffusion of solute atoms to mobile dislocations. Type-C serrations are attributed to unlocking of temporarily arrested forest dislocations in solute atmospheres and dissociation of full dislocations due to Suzuki segregation, and are associated with discontinuous PLC band propagations. Thus, type-C serrations feature downward spikes below the mean level of flow stress in the true stress-true strain curves, as shown in Fig. 3b and c.

By examining the plastic flow of the MEA within the temperature range between 25 °C and 1000 °C (Fig. 2a), it can be concluded that the presence of DSA has a dramatic impact on tensile properties of the $Ni_2Co_1Fe_1V_{0.5}Mo_{0.2}$ MEA. At 25 °C, solute diffusion rate is too low to activate DSA, therefore the solid solution strengthening effect is very strong, benefiting the tensile properties, while other factors also contribute more or less in a positive manner. The negative SRS, type-A and type-C serrations occurred at 400 °C to 700 °C are attributed to DSA of forest dislocations [25]. The positive SRS, increasing SRS with increasing strain and sole type-B serrations at 800 °C are attributed to DSA of mobile dislocations. Above 900 °C (significantly higher than 0.6Tm), the solute atoms become sufficiently mobile to move with dislocations resulting in ineffective or no locking of dislocations and thus disappearance of serrations. Hence, the DSA effect on mechanical properties becomes negligible at such a high temperature.

Secondly, another generalized parameter, the activation volume shows an inverse trend in comparison to the SRS-temperature dependence. The magnitude of activation volume is also often used to differentiate various deformation mechanisms [61]. According to literatures [47,48,62], the activation volume at room temperature for point defect migration is 0.02 b^3-0.1 b^3, for diffusional creep is ~1 b^3, for kink pairs on gliding screw dislocations in bcc metals is 1 b^3-10 b^3, for dislocation-twin interactions is 1-100 b^3, for dislocation cross-slip at obstacles is 50 b^3- 300 b^3 and for forest dislocation cutting is 1000 b^3 and higher.

For the $Ni_2Co_1Fe_1V_{0.5}Mo_{0.2}$ MEA tensile deformed at 25 °C, the activation volume is steady within the range of 69.3 b^3 to 104.7 b^3, as shown in Fig. 5b, suggesting frequent short-range solute pinning [48] and cross-slip of dislocations due to combined effect of massive dislocation pile-up [1] and LCO [4]. For the MEA deformed in the temperature range between 400 °C and 700 °C, the activation volume fluctuates within the range between 380 b^3 and 2760

b^3, suggesting long-range bowing of the dislocation lines [48] and the dominance of forest dislocation cutting mechanism. Thus, both negative SRS and high activation volume support the dominance of forest strengthening mechanism at the temperatures from 400 °C to 700 °C. At 800 °C, the activation volume decreases with increasing strain from 5910 b^3 to 162 b^3, suggesting increased tendency for cross-slip of screw dislocations over the forest dislocation cutting mechanism with increasing strain [62].

It is well known that the strain hardening capacity determines the σ_{UTS} and ductility of metallic materials [63]. In despite of the decreasing trends of strength and ductility with respect to the increasing temperature, the $Ni_2Co_1Fe_1V_{0.5}Mo_{0.2}$ MEA still shows excellent strength-ductility combination in the temperature range between 25°C and 800°C, as shown Fig. 2. This is attributed to the remarkable dislocation storage capacity and high strain hardening rate of the MEA. The strain hardening exponent (n) of the MEA is as high as ~1.15 at 25 °C, and moderately decreases with increasing temperature to ~0.9 at 800 °C, as shown in Fig. 4f. A large n value is the indicator for the large dislocation storage capacity, which enhances ductility and delays the onset of necking. For pure fcc metals, such as a coarse-grained Cu, its n value is only ~0.35 [64]. Even for a nano-twined Cu, in which an enormous amount of twin boundaries (TBs) is available for dislocation storage, its n value is only ~0.66 [65]. Apparently, the multi-principal element (concentrated solid solution) design of the $Ni_2Co_1Fe_1V_{0.5}Mo_{0.2}$ MEA significantly increased the dislocation storage capacity which is reflected by the high n value above 0.9 [13].

As shown in Fig. 2d, all the MEA samples show up-turn of strain hardening rates short after the elasto-plastic transition region, in the temperature range between 25°C and 800°C. This phenomenon is remarkable, because conventional polycrystalline metallic materials usually show monotonous decrease in strain hardening rates (stage III strain hardening) after the elasto-plastic transition region. To date only some particular metallic materials have demonstrated the up-turn for strain hardening rates [66-70]. The up-turn of strain hardening rate has been attributed to the twinning-induced plasticity (TWIP) effect [66], transformation-induced plasticity (TRIP) effect [68] and hetero-deformation induced (HDI) hardening effect [71]. TWIP and TRIP effects instantly generate additional boundaries for dislocation storage and significantly reduce the effective grain size, resulting in up-turn of strain hardening rate [66-68,72,73]. Previously reported HDI hardening effect requires hetero-structure to exert strong back stress to stimulate additional geometrically necessary dislocations (GNDs) for secondary strain hardening (up-turn of strain hardening rate) [74]. However, the MEA studied here has neither TWIP/TRIP effect or hetero-structure. Thus, there has to be another reason for the up-turn of strain hardening rate. Like other obstacles a dislocation forest can also exert back stress to dislocations [25]. Although, the dislocation forest is far less effective than GB and TB for blocking dislocations, a high density of dislocation forests with solute atmospheres in concentrated solid solution is considered sufficient for back stress strengthening, thus causing the up-turn of strain hardening rate. The negative SRS and the activation volume higher than 1000 b^3 indicate the dominance of forest strengthening mechanism at the temperatures from 400 °C to 700 °C [62,75]. In fact, forest dislocations govern the strain hardening of the MEA throughout the temperature range from 25 °C to 800 °C, proved by microstructural analysis in the following section. It is worth to note that dislocation slip in HEA and MEA has to continuously overcome the activation barriers created by SRO and/or incipient concentration waves, and thus the dislocation motion is slowed down [1,4,5]. As a result, the up-turn of strain hardening rate is not sharp but spans in a large strain range as shown in Fig. 2d.

Strain hardening in single phase HEAs and MEAs are affected by three correlated microstructural features – lattice distortion, LCO

(such as SRO and/or incipient concentration waves) and dislocation forest [4,76]. The degree of atomic size mismatch between constituent elements directly influences lattice distortion, LCO and the barrier strength of dislocation forest, thus in turn affects the critical stress for dislocation slip and dislocation storage capacity in the bulk material [1,4,20]. It requires sophisticated experiments and simulations to unveil the effect of elemental composition on atomic size mismatch, lattice distortion and LCO, which is beyond the scope of this work. As an alternative, an experimental work based on stress-strain response of bulk materials has been conducted to show the influence of atomic size mismatch on the strain hardening behavior. The five constituent elements in the pioneering NiCrMnFeCo Cantor alloy have similar atomic radius, and thus the atomic size mismatch is small. The stress-strain response and work hardening behavior of the Cantor alloy are taken as the reference, as shown in Fig. S2 in the supplementary material. Dislocation slip in the Cantor alloy has to continuously overcome the activation barriers created by lattice distortion, LCO and dislocation forests [1,4,20]. As a result, the strain hardening rate levels off after elasto-plastic transition for the Cantor alloy [55]. In contrast, Mo and V have much larger atomic radius than Fe, Co and Ni, thus the addition of Mo and V can pose much larger atomic size mismatch than that attained in the Cantor alloy. In turn, the activation barriers created by lattice distortion, LCO and dislocation forests for dislocation slip are expected to be higher in the $Ni_2Co_1Fe_1V_{0.5}Mo_{0.2}$ MEA. As a result, there is an up-turn of strain hardening rate for the $Ni_2Co_1Fe_1V_{0.5}Mo_{0.2}$ MEA as shown in Fig. 2d and Fig. S1. This result directly shows that increasing the atomic size mismatch in HEAs and MEAs by adding elements of significantly different atomic radii can substantially increase the strain hardening capacity.

4.2. Temperature dependence of deformation mechanisms

After analyzing the generalized parameters m and ΔV^*, it is now clear that the evolution of forest dislocations during plastic deformation governs the mechanical properties of the $Ni_2Co_1Fe_1V_{0.5}Mo_{0.2}$ MEA. However, dislocation forest can possess different configurations and strength depends on the types of constituent dislocations. As shown in Fig. 6a, planar dislocations, featuring long and straight lines on {111} planes, formed mosaic patterns. Curved and straight dislocations are tangled to form forest structures. According to Fig. 8, the dislocation density is the highest and the fraction of pure screw dislocations is the lowest at 25 °C. Provided that an edge dislocation has a much larger strain field than a screw dislocation with the same Burgers vector [77], the dislocation forest formed at 25 °C is a much stronger obstacle than that formed at higher temperatures. In addition, the solute atoms are relatively immobile, and DSA is inactive. Hence, the $Ni_2Co_1Fe_1V_{0.5}Mo_{0.2}$ MEA has excellent mechanical properties at 25 °C, as shown in Fig. 2a.

When the deformation temperature is increased to the range between 400 °C and 700 °C, the amounts of curved dislocations increased as shown in Fig. 6b to f. Dislocations in planar array and dipole configurations are formed due to SRO at elevated temperature. Although the overall stacking fault energy of the bulk alloy tends to increase with increasing temperature [78], SFs are observed at elevated temperature. Both literatures and observed Type-C serrations in Fig. 3b and c, support that the SFs are attributed to Suzuki segregation [79]. Curved dislocations usually possess screw components, and thus are likely to cross slip and tangle with other dislocations to form dislocation forest. Dislocation dipoles, planar arrays and SFs are low energy configurations which tend to pile up at obstacles. Despite of different dislocation configurations, the dislocation densities at 400 °C to 700 °C are lower than that at 25 °C, the shear modulus is lowered due

to increased temperature, and DSA is active to deteriorate homogeneous deformation. As the combined result, the strength, ductility and strain hardening rate at elevated temperatures are reduced, as shown in Fig. 2a and b. It is worth to note that the up-turn of strain hardening rate at 400 °C to 600 °C are similar, but decreased dramatically at 700 °C, as revealled in Fig. 2d. This is attributed to the dramatic increase in the fraction of screw dislocations when the temperature is increased from 600 °C to 700 °C, as shown in Fig. 8. At elevated temperatures, the line tension of dislocation decreases due to reduced shear modulus, thus the length of dislocation increases [24]. For a long screw dislocation segment, the effective energy barrier for cross-slip is lowered under shear stress, according to a weak-link scaling relationship [80]. As a result, a screw dislocation in the fcc structure can easily cross slip to an intercepting slip plane when it encounters an obstacle such as a dislocation forest, at elevated temperatures. Pronounced dislocation cross-slip reduces the number of dislocations in the piled-up, and hence the long-range back stress is reduced. Moreover, cross-slip of dislocations can lead to annihilation of screw dipoles, which also reduces the local back stress. Therefore, increased fraction of screw dislocations with strong propensity to cross slip significantly reduced the strain hardening rate of the MEA at 700 °C, as shown in Fig. 2d.

At 800 °C, long and curly dislocations dominate plastic deformation as shown in Fig. 7a and b and Fig. 8. Surprisingly, the $Ni_2Co_1Fe_1V_{0.5}Mo_{0.2}$ MEA still shows strong up-turn of strain hardening rate after the elasto-plastic transition, as shown in Fig. 2d. As mentioned earlier, type-B serrations with high magnitude and frequency dominate the plastic flow (Fig. 3d), and jump up in strain rate instantaneously increases the flow stress (Fig. 5a), indicating that solute pinning effect is still strong and mobile dislocation aging is in dominance. At such a high temperature, although a jump up in strain rate could still accelerate the production of new forest dislocations, the average forest is younger and less-aged than the majority of mobile dislocations. Therefore, forest aging mechanism is retarded [25]. Meanwhile, the activation volume decreases from 5910 b^3 to 162 b^3 with increasing strain, indicating that the deformation mechanism changes from forest cutting to cross-slip. Fig. 7b clearly shows that long and curved dislocations are cutting each other at multiple intersections [62]. According to above-mentioned results, the stronger up-turn of strain hardening rate for the MEA at 800 °C than that at 700 °C can be explained as follows: (1) After elasto-plastic transition the plastic flow is accommodated by a sharp increase in forest dislocation density ($\Delta V^* = 5910\ b^3$); The solute drag effect (type-B serrations, positive m) posed on elongated dislocation lines enhanced the forest dislocation strengthening effect, and thus led to the sharp up-turn of strain hardening rate. (2) As the flow stress increases with increasing strain, cross-slip of screw dislocations quickly takes dominance ($\Delta V^* = 162\ b^3$), leading to recovery/annihilation of dislocations and thus earlier decline in strain hardening rate comparing to the MEA deformed at lower temperatures (Fig. 2d).

4.3. Temperature dependence of fracture mechanisms

Within the temperature range of 25 °C to 1000 °C, the shear fracture angles are in the range between 45° and 90°. According to the Ellipse criterion proposed by Zhang et al., the ratio of the critical normal fracture stress σ_0 to the shear fracture stress τ_0 of the material shall satisfy the condition of $0 < \tau_0/\sigma_0 < \sqrt{2}/2$ [81]. Thus, the tensile failure mode of the MEA matches the Mohr-Coulomb criteria and von Mises criteria, suggesting that the failure mode is governed by dislocation activities. This is also verified by the analysis of m, ΔV^*, serrated flow and microstructures.

The fracture tip is the region of global strain localization, where deformation structures associated with plastic instability are ap-

parent [82]. Firstly, wavy cracks on the lateral surfaces are observed. These cracks are associated with slip bands in which high densities of dislocations glide at high velocities towards the surface of the bulk material. Usually, slip bands create sharp steps on the surface of a bulk material. However, wavy cracks are shown in Fig. 9 a-1, b-1, c-1 and Fig. 10 b-1. Particularly, the cracks appeared on the lateral surface of the fracture tip of the 900 °C sample are wide and jagged, resembles the crevices formed on a semidried bread dough when it is pulled. This is because the enthalpy of the MEA is very high at such a high temperature. Correspondingly, the ductility of the MEA is governed by the strong mobility of atoms, dislocation forest and dynamic recovery. When massive dislocations reached the surface to form the macroscopic slip bands, many micro-voids of various sizes also formed due to the high strain carried by the entangled dislocations on the "mushy" surface. As plastic deformation proceeds, micro-voids coalesced on the surface to form the jagged cracks.

Secondly, top views of the fracture tips illustrated in Fig. 9 a-3, b-3 and c-3, show micrometer size circular dimples, indicating ductile fracture associated with dislocation cells at the temperatures up to 600 °C. However, cleavage planes of various orientations are observed at 700 °C, shown in Fig. 9 d-3. As shown in Fig. 6e, dislocation wall/forest are strongly confined on slip planes. Meanwhile, pronounced forest aging causes significant solute segregation to the slip planes, as indicated by the negative SRS. Therefore, the slip planes containing high densities of forest dislocations in the current case are embrittled by massive segregation, resulting in the micrometer sized cleavage planes [55] and apparently dropped σ_{UTS} and ductility (Fig. 2b).

As shown in Fig. 10 a-3, b-3 and c-3, fine spheres formed on the dimple surfaces at 800 °C, and globules formed instead of dimples at 900 °C and 1000 °C. The images indicate that partial melting occurred at the fracture tips when the test temperature is 800 °C and higher. The thermal expansion is very large at 1000 °C, therefore globules cracked after cooling due to thermal contraction (Fig. 10 c-3). Moderate melting of fracture debris (Fig. 10 a-3) and apparent secondary strain hardening effect occurred at 800 °C, indicating that 800 °C which is above $0.6Tm$ of the $Ni_2Co_1Fe_1V_{0.5}Mo_{0.2}$ MEA is about the upper limit for strain hardening.

5. Conclusion

A $Ni_2Co_1Fe_1V_{0.5}Mo_{0.2}$ MEA with the fcc crystal structure was produced by medium frequency induction melting technique. The influence of temperature on the tensile properties of the as-cast $Ni_2Co_1Fe_1V_{0.5}Mo_{0.2}$ MEA was studied in the temperature range of 25-1000 °C. Based on detailed experimental work and analysis, several conclusions can be drawn as follows:

1) The multi-principal element design of the $Ni_2Co_1Fe_1V_{0.5}Mo_{0.2}$ MEA grants the material with an ultra-high dislocation storage capacity ($n > 0.9$) and a very strong solid solution strengthening effect. As a result, the as-cast MEA possesses an outstanding combination of strength and ductility, and the secondary strain hardening capability at the test temperatures up to 800 °C.

2) At 25 °C, the as-cast $Ni_2Co_1Fe_1V_{0.5}Mo_{0.2}$ MEA has a σ_{UTS} of 583 MPa and a ε_u of 58%. The outstanding strain hardening behavior of the MEA is attributed to strong short-range solute pinning effect, massive dislocation pile-up and absence of DSA.

3) At the temperatures between 400 °C and 700 °C, negative SRS, type-A and type-C serrations are detected by the tensile tests. Low energy configurations including dislocation dipoles, planar arrays and SFs formed during plastic deformation. While the low energy dislocation structures benefit the mechanical properties, DSA of forest dislocations deteriorate the ductility, re-

sulting in a decreasing trend of both strength and ductility with increasing temperature.

4) Even at 800 °C, the MEA still possesses an apparent secondary strain hardening effect, and a high σ_{UTS} of 320 MPa, due to still effective solid solution strengthening and forest strengthening effects. The positive SRS, increasing SRS with increasing strain and sole type-B serrations at 800 °C are attributed to DSA of mobile dislocations. With increasing strain, the dominant deformation mechanism changes from forest dislocation cutting mechanism to dislocation cross-slip, resulting in the sharp upturn of strain hardening rate.

5) At the temperature above 900 °C (significantly higher than $0.6Tm$), the solute atoms become sufficiently mobile to move with dislocations, resulting in ineffective or no locking of dislocations and thus disappearance of serrations. Large thermal energy input accelerates recovery and recrystallisation, which offset the strain hardening effect, leading to strain softening right after yielding.

To sum up, the as cast $Ni_2Co_1Fe_1V_{0.5}Mo_{0.2}$ MEA possesses outstanding mechanical properties including strain hardening capacity at room temperature and at high temperatures up to 800°C in comparison with many other alloys. The experimental results indicate that the addition of V and Mo is the key to improve the mechanical properties of the alloy in the current case. The fundamental idea is that adding elements with significantly different atomic sizes can alter the lattice distortion, LCO and dislocation forests, thus to impede dislocation slip and increase dislocation storage. Therefore, a high strain hardening capacity is attained by the massive accumulation of dislocations, as long as the solute pinning effect is still active, even at high temperatures. This discovery provides guidance for designing single phase HEAs and MEAs with outstanding strain hardening capacity and high temperature mechanical properties.

Author Contributions

Conceptualization, supervision – Yonghao Zhao; Writing, review and editing – Yonghao Zhao and Yang Cao; Data curation, visualization, writing - original draft – Wei Jiang; Validation, formal analysis – Yong Zhang and Yang Cao; Investigation – Wei Jiang and Shengyun Yuan; Funding acquisition – Yonghao Zhao, Yang Cao and Yong Zhang. All authors have read and agreed to the published version of the manuscript.

Declaration of competing interest

The authors declare no conflict of interest.

Supplementary materials

Supplementary material associated with this article can be found, in the online version, at doi:10.1016/j.actamat.2021.116982.

References

[1] Q.Q. Ding, Y. Zhang, X. Chen, X.Q. Fu, D.K. Chen, S.J. Chen, L. Gu, F. Wei, H.B. Bei, Y.F. Gao, M.R. Wen, J.X. Li, Z. Zhang, T. Zhu, R.O. Ritchie, Q. Yu, Tuning element distribution, structure and properties by composition in high-entropy alloys, Nature 574 (2019) 223–227.

[2] B. Gludovatz, A. Hohenwarter, K.V.S. Thurston, H.B. Bei, Z.G. Wu, E.P. George, R.O. Ritchie, Exceptional damage-tolerance of a medium-entropy alloy CrCoNi at cryogenic temperatures, Nat. Commun. 7 (2016) 10602.

[3] O.N. Senkov, J.D. Miller, D.B. Miracle, C. Woodward, Accelerated exploration of multi-principal element alloys with solid solution phases, Nat. Commun. 6 (2015) 6529.

[4] Q.J. Li, H. Sheng, E. Ma, Strengthening in multi-principal element alloys with local-chemical-order roughened dislocation pathways, Nat. Commun. 10 (2019) 3563.

[5] Z.J. Zhang, M.M. Mao, J.W. Wang, B. Gludovatz, Z. Zhang, S.X. Mao, E.P. George, Q. Yu, R.O. Ritchie, Nanoscale origins of the damage tolerance of the high-entropy alloy CrMnFeCoNi, Nat. Commun. 6 (2015) 10143.

[6] J.W. Yeh, S.K. Chen, S.J. Lin, J.Y. Gan, T.S. Chin, T.T. Shun, C.H. Tsau, S.Y. Chang, Nanostructured high-entropy alloys with multiple principal elements: novel alloy design concepts and outcomes, Adv. Eng. Mater. 6 (2004) 299–303.

[7] B. Cantor, I.T.H. Chang, P. Knight, A.J.B. Vincent, Microstructural development in equiatomic multicomponent alloys, Mater. Sci. Eng. A 375-377 (2004) 213–218.

[8] Y. Zhang, T.T. Zuo, Z. Tang, M.C. Gao, K.A. Dahmen, P.K. Liaw, Z.P. Lu, Microstructures and properties of high-entropy alloys, Prog. Mater. Sci. 61 (2014) 1–93.

[9] D. Miracle, J. Miller, O. Senkov, C. Woodward, M. Uchic, J. Tiley, Exploration and development of high entropy alloys for structural applications, Entropy 16 (2014) 494–525.

[10] X.F. Chen, Q. Wang, Z.Y. Cheng, M.L. Zhu, H. Zhou, P. Jiang, L.L. Zhou, Q.Q. Xue, F.P. Yuan, J. Zhu, X.L. Wu, E. Ma, Direct observation of chemical short-range order in a medium-entropy alloy, Nature 592 (2021) 712–716.

[11] R.P. Zhang, S.T. Zhao, J. Ding, Y. Chong, T. Jia, C. Ophus, M. Asta, R.O. Ritchie, A.M. Minor, Short-range order and its impact on the CrCoNi medium-entropy alloy, Nature 581 (2020) 283–287.

[12] K.Y. Tsai, M.H. Tsai, J.W. Yeh, Sluggish diffusion in Co-Cr-Fe-Mn-Ni high-entropy alloys, Acta Mater 61 (2013) 4887–4897.

[13] J.W. Yeh, S.Y. Chang, Y.D. Hong, S.K. Chen, S.J. Lin, Anomalous decrease in X-ray diffraction intensities of Cu-Ni-Al-Co-Cr-Fe-Si alloy systems with multi-principal elements, Mater. Chem. Phys. 103 (2007) 41–46.

[14] L.J. Santodonato, Y. Zhang, M. Feygenson, C.M. Parish, M.C. Gao, R.J. Weber, J.C. Neuefeind, Z. Tang, P.K. Liaw, Deviation from high-entropy configurations in the atomic distributions of a multi-principal-element alloy, Nat. Commun. 6 (2015) 5964.

[15] P. Kozelj, S. Vrtnik, A. Jelen, S. Jazbec, Z. Jaglicic, S. Maiti, M. Feuerbacher, W. Steurer, J. Dolinsek, Discovery of a superconducting high-entropy alloy, Phys. Rev. Lett. 113 (2014) 107001.

[16] N. Park, I. Watanabe, D. Terada, Y. Yokoyama, P.K. Liaw, N. Tsuji, Recrystallization behavior of CoCrCuFeNi high-entropy alloy, Metall. Mater. Trans. A 46 (2014) 1481–1487.

[17] J.H. Kim, Y.S. Na, Tensile properties and serrated flow behavior of as-cast CoCrFeMnNi high-entropy alloy at room and elevated temperatures, Met. Mater. Int. 25 (2018) 296–303.

[18] J.X. Fu, C.M. Cao, W. Tong, Y.X. Hao, L.M. Peng, The tensile properties and serrated flow behavior of a thermomechanically treated CoCrFeNiMn high-entropy alloy, Mater. Sci. Eng. A 690 (2017) 418–426.

[19] A. Gali, E.P. George, Tensile properties of high- and medium-entropy alloys, Intermetallics 39 (2013) 74–78.

[20] F. Otto, A. Dlouhý, C. Somsen, H. Bei, G. Eggeler, E.P. George, The influences of temperature and microstructure on the tensile properties of a CoCrFeMnNi high-entropy alloy, Acta Mater 61 (2013) 5743–5755.

[21] A.V. Kuznetsov, D.G. Shaysultanov, N.D. Stepanov, G.A. Salishchev, O.N. Senkov, Tensile properties of an AlCrCuNiFeCo high-entropy alloy in as-cast and wrought conditions, Mater. Sci. Eng. A 533 (2012) 107–118.

[22] H.M. Daoud, A.M. Manzoni, N. Wanderka, U. Glatzel, High-temperature tensile strength of $Al_{10}Co_{25}Cr_8Fe_{15}Ni_{36}Ti_6$ compositionally complex alloy (high-entropy alloy), Jom 67 (2015) 2271–2277.

[23] D. Caillard, Dynamic strain ageing in iron alloys: The shielding effect of carbon, Acta Mater 112 (2016) 273–284.

[24] Z. Wu, H. Bei, G.M. Pharr, E.P. George, Temperature dependence of the mechanical properties of equiatomic solid solution alloys with face-centered cubic crystal structures, Acta Mater 81 (2014) 428–441.

[25] M.A. Soare, W.A. Curtin, Solute strengthening of both mobile and forest dislocations: The origin of dynamic strain aging in fcc metals, Acta Mater 56 (2008) 4046–4061.

[26] F. Zhang, A.F. Bower, W.A. Curtin, The influence of serrated flow on necking in tensile specimens, Acta Mater 60 (2012) 43–50.

[27] M. Kolluri, P.t. Pierick, T. Bakker, Characterization of high temperature tensile and creep-fatigue properties of Alloy 800H for intermediate heat exchanger components of (V)HTRs, Nucl. Eng. Des. 284 (2015) 38–49.

[28] T.J. Zhou, H.S. Ding, X.P. Ma, W. Feng, H.B. Zhao, A.L. Li, Y. Meng, H.X. Zhang, Effect of precipitates on high-temperature tensile strength of a high W-content cast Ni-based superalloy, J. Alloys Compd. 797 (2019) 486–496.

[29] D. Kaoumi, K. Hrutkay, Tensile deformation behavior and microstructure evolution of Ni-based superalloy 617, J. Nucl. Mater. 454 (2014) 265–273.

[30] G. Chen, Y. Peng, G. Zheng, Z. Qi, M. Wang, H. Yu, C. Dong, C.T. Liu, Polysynthetic twinned TiAl single crystals for high-temperature applications, Nat. Mater. 15 (2016) 876–881.

[31] F. Appel, M. Oehring, J.D.H. Paul, A novel in situ composite structure in TiAl alloys, Mater. Sci. Eng. A 493 (2008) 232–236.

[32] H.X. Pei, S.L. Li, L.X. Wang, H.L. Zhang, Z.D. Zhao, X.T. Wang, Influence of Initial Microstructures on Deformation Behavior of 316LN Austenitic Steels at 400-900°C, J. Mater. Eng. Perform. 24 (2014) 694–699.

[33] H.X. Pei, H.L. Zhang, L.X. Wang, S.L. Li, D.Z. Li, X.T. Wang, Tensile behaviour of 316LN stainless steel at elevated temperatures, Mater, High Temp 31 (2014) 198–203.

[34] H.Q. Dong, L.M. Yu, Y.C. Liu, C.X. Liu, H.J. Li, J.F. Wu, Effect of hafnium addition on the microstructure and tensile properties of aluminum added high-Cr ODS steels, J. Alloys Compd. 702 (2017) 538–545.

[35] R.L. Klueh, J.P. Shingledecker, R.W. Swindeman, D.T. Hoelzer, Oxide dispersion-strengthened steels: A comparison of some commercial and experimental alloys, J. Nucl. Mater. 341 (2005) 103–114.

[36] S. Yokoshima, M. Yamaguchi, Fracture behavior and toughness of PST crystals of TiAl, Acta Mater 44 (1996) 873–883.

[37] D.R. Johnson, Y. Masuda, H. Inui, M. Yamaguchi, Alignment of the TiAl/Ti3Al lamellar microstructure in TiAl alloys by growth from a seed material, Acta Mater 45 (1997) 2523–2533.

[38] J.R. Li, C.L. Zhang, Y.Z. Liu, Influence of carbides on the high-temperature tempered martensite embrittlement of martensitic heat-resistant steels, Mater. Sci. Eng. A 670 (2016) 256–263.

[39] L. Jiang, Y.P. Lu, M. Song, C. Lu, K. Sun, Z.Q. Cao, T.M. Wang, F. Gao, L.M. Wang, A promising $CoFeNi_2V_{0.5}Mo_{0.2}$ high entropy alloy with exceptional ductility, Scr. Mater. 165 (2019) 128–133.

[40] L. Jiang, D.X. Qiao, Z.Q. Cao, C.Y. Lu, M. Song, L.M. Wang, Tunable mechanical property and strain hardening behavior of a single-phase $CoFeNi_2V_{0.5}Mo_{0.2}$ high entropy alloy, Mater. Sci. Eng. A 776 (2020) 139027.

[41] P.W. Trimby, Y. Cao, Z.B. Chen, S. Han, K.J. Hemker, J.S. Lian, X.Z. Liao, P. Rottmann, S. Samudrala, J.L. Sun, J.T. Wang, J. Wheeler, J.M. Cairney, Characterizing deformed ultrafine-grained and nanocrystalline materials using transmission Kikuchi diffraction in a scanning electron microscope, Acta Mater 62 (2014) 69–80.

[42] L.L. Han, X.D. Xu, Z.M. Li, B. Liu, C.T. Liu, Y. Liu, A novel equiaxed eutectic high-entropy alloy with excellent mechanical properties at elevated temperatures, Mater. Res. Lett. 8 (2020) 373–382.

[43] M.M. Li, M. Zu, Y. Yu, W.C. Zhang, Elevated temperature tensile behavior and microstructure evolution of liquid phase sintered 90W-7Ni-3Fe alloy, J. Alloys Compd. 802 (2019) 528–534.

[44] H.W. Wang, J.Q. Qi, C.M. Zou, D.D. Zhu, Z.J. Wei, High-temperature tensile strengths of in situ synthesized TiC/Ti-alloy composites, Mater. Sci. Eng. A 545 (2012) 209–213.

[45] G.W. Han, I.P. Jones, R.E. Smallman, Direct evidence for Suzuki segregation and Cottrell pinning in MP159 superalloy obtained by FEG(S)TEM/EDX, Acta Mater 51 (2003) 2731–2742.

[46] J.P. Hirth, J. Lothe, Theory of dislocations, second ed., Krieger Pub, MalabarFL, 1992.

[47] Y.M. Wang, A.V. Hamza, E. Ma, Temperature-dependent strain rate sensitivity and activation volume of nanocrystalline Ni, Acta Mater 54 (2006) 2715–2726.

[48] Z.G. Wu, Y.F. Gao, H.B. Bei, Thermal activation mechanisms and Labusch-type strengthening analysis for a family of high-entropy and equiatomic solid-solution alloys, Acta Mater 120 (2016) 108–119.

[49] B. Banerjee, The mechanical threshold stress model for various tempers of AISI 4340 steel, Int. J. Solids Struct. 44 (2007) 834–859.

[50] Y.Q. Sun, Line tension of screw dislocations on cross-slip planes, Philos. Mag. Lett. 74 (2010) 175–188.

[51] H. Siethoff, Cross-slip in the high-temperature deformation of germanium, silicon and indium antimonide, Philos. Mag. A 47 (2006) 657–669.

[52] R.K. Ham, The determination of dislocation densities in thin films, Philos. Mag. A 6 (1961) 1183–1184.

[53] F.J. Humphreys, M. Hatherly, Recrystallization and related annealing phenomena, second ed., Elsevier, Oxford, 2004.

[54] H.P.Karnthaler Gerold, On the origin of planar slip in f.c.c. alloys, Acta Metall 37 (1989) 2177–2183.

[55] K.S. Ming, L.L. Li, Z.M. Li, X.F. Bi, J. Wang, Grain boundary decohesion by nanoclustering Ni and Cr separately in CrMnFeCoNi high-entropy alloys, Sci. Adv. 5 (2019) eaay0639.

[56] E.W. Hart, Theory of the tensile test, Acta Metall. 15 (1967) 351–355.

[57] S.H. Fu, T. Cheng, Q.C. Zhang, Q. Hu, P.T. Cao, Two mechanisms for the normal and inverse behaviors of the critical strain for the Portevin-Le Chatelier effect, Acta Mater 60 (2012) 6650–6656.

[58] W.A. Curtin, D.L. Olmsted, L.G. Hector, A predictive mechanism for dynamic strain ageing in aluminium-magnesium alloys, Nat. Mater. 5 (2006) 875–880.

[59] T. Mäkinen, P. Karppinen, M. Ovaska, L. Laurson, M.J. Alava, Propagating bands of plastic deformation in a metal alloy as critical avalanches, Sci. Adv. 6 (2020) eabc7350.

[60] B.K. Choudhary, Influence of strain rate and temperature on serrated flow in 9Cr-1Mo ferritic steel, Mater. Sci. Eng. A 564 (2013) 303–309.

[61] P. Rodriguez, Grain size dependence of the activation parameters for plastic deformation Influence of crystal structure, slip system, and rate-controlling dislocation mechanism, Metall. Mater. Trans. A 35A (2004) 2697–2705.

[62] W. Püschl, Models for dislocation cross-slip in close-packed crystal structures: a critical review, Prog. Mater. Sci. 47 (2002) 415–461.

[63] I.A. Ovid'ko, R.Z. Valiev, Y.T. Zhu, Review on superior strength and enhanced ductility of metallic nanomaterials, Prog. Mater. Sci. 94 (2018) 462–540.

[64] A. Misra, X. Zhang, D. Hammon, R.G. Hoagland, Work hardening in rolled nanolayered metallic composites, Acta Mater 53 (2005) 221–226.

[65] L. Lu, Z.S. You, K. Lu, Work hardening of polycrystalline Cu with nanoscale twins, Scr. Mater. 66 (2012) 837–842.

[66] I. Gutierrez-Urrutia, D. Raabe, Dislocation and twin substructure evolution during strain hardening of an Fe-22wt.% Mn-0.6wt.% C TWIP steel observed by electron channeling contrast imaging, Acta Mater 59 (2011) 6449–6462.

[67] J. Su, D. Raabe, Z.M. Li, Hierarchical microstructure design to tune the mechanical behavior of an interstitial TRIP-TWIP high-entropy alloy, Acta Mater 163 (2019) 40–54.

[68] T.S. Byun, N. Hashimoto, K. Farrell, Temperature dependence of strain hardening and plastic instability behaviors in austenitic stainless steels, Acta Mater 52 (2004) 3889–3899.

[69] X.L. Wu, P. Jiang, L. Chen, F.P. Yuan, Y.T. Zhu, Extraordinary strain hardening by gradient structure, Proc. Natl. Acad. Sci. 111 (2014) 7197–7201.

[70] X.L. Wu, M.X. Yang, F.P. Yuan, G.L. Wu, Y.J. Wei, X.X. Huang, Y.T. Zhu, Heterogeneous lamella structure unites ultrafine-grain strength with coarse-grain ductility, Proc. Natl. Acad. Sci. 112 (2015) 14501–14505.

[71] Y.T. Zhu, X.L. Wu, Perspective on hetero-deformation induced (HDI) hardening and back stress, Mater. Res. Lett. 7 (2019) 393–398.

[72] Y.T. Zhu, X.Z. Liao, X.L. Wu, Deformation twinning in nanocrystalline materials, Prog. Mater. Sci. 57 (2012) 1–62.

[73] I. Gutierrez-Urrutia, D. Raabe, Grain size effect on strain hardening in twinning-induced plasticity steels, Scr. Mater. 66 (2012) 992–996.

[74] Y.T. Zhu, K. Ameyama, P.M. Anderson, I.J. Beyerlein, H.J. Gao, H.S. Kim, E. Lavernia, S. Mathaudhu, H. Mughrabi, R.O. Ritchie, N. Tsuji, X.Y. Zhang, X.L. Wu, Heterostructured materials: superior properties from hetero-zone interaction, Mater. Res. Lett. 9 (2020) 1–31.

[75] X.Z. Gao, Y.P. Lu, J.Z. Liu, J. Wang, T.M. Wang, Y.H. Zhao, Extraordinary ductility and strain hardening of $Cr_{26}Mn_{20}Fe_{20}Co_{20}Ni_{14}$ TWIP high-entropy alloy by cooperative planar slipping and twinning, Materialia 8 (2019) 100485.

[76] E. Antillon, C. Woodward, S.I. Rao, B. Akdim, T.A. Parthasarathy, Chemical short range order strengthening in a model FCC high entropy alloy, Acta Mater 190 (2020) 29–42.

[77] C.H. Henager, R.G. Hoagland, Dislocation core fields and forces in fcc metals, Scr. Mater. 50 (2004) 1091–1095.

[78] S. Curtze, V.T. Kuokkala, Dependence of tensile deformation behavior of TWIP steels on stacking fault energy, temperature and strain rate, Acta Mater 58 (2010) 5129–5141.

[79] Y. Koizumi, T. Nukaya, S. Suzuki, S. Kurosu, Y.P. Li, H. Matsumoto, K. Sato, Y. Tanaka, A. Chiba, Suzuki segregation in Co-Ni-based superalloy at 973K: An experimental and computational study by phase-field simulation, Acta Mater 60 (2012) 2901–2915.

[80] W.G. Nöhring, W.A. Curtin, Cross-slip of long dislocations in fcc solid solutions, Acta Mater 158 (2018) 95–117.

[81] Z.F. Zhang, J. Eckert, Unified tensile fracture criterion, Phys. Rev. Lett. 94 (2005) 094301.

[82] Y.F. Liu, Y. Cao, Q.Z. Mao, H. Zhou, Y.H. Zhao, W. Jiang, Y. Liu, J.T. Wang, Z.S. You, Y.T. Zhu, Critical microstructures and defects in heterostructured materials and their effects on mechanical properties, Acta Mater 189 (2020) 129–144.